Authors' accepted manuscript
Article published in Journal of Materials in Civil Engineering, Vol. 35, no 7, 2023.
The final published version available at http://dx.doi.org/10.1061/JMCEE7.MTENG-15024

Microstructure Characterization of Cement Paste with Treated Spent Pot Lining Recycled From Primary Aluminum Production

Hang Tran[1], Luca Sorelli[2*], Victor Brial[3], David Conciatori[4], Claudiane Ouellet-Plamondon[5]

[1] Ph.D student, Department of Civil and Water Engineering, Laval Université, 1065 avenue de la Médecine, G1V 0A6, Québec, Canada. Email: thi-hang.tran.1@ulaval.ca

[2] Professor, Department of Civil and Water Engineering, Laval Université, 1065 avenue de la Médecine, G1V 0A6, Québec, Canada (**corresponding author*). Email: luca.sorelli@gci.ulaval.ca

[3] Ph.D student, Department of Construction Engineering, École de Technologie Supérieure, 1100 rue Notre-Dame Ouest, H3C1K3, Montréal, Canada. Email: victor.brial.1@ens.etsmtl.ca

[4] Associate Professor, Department of Civil and Water Engineering, Laval Université, 1065 avenue de la Médecine, G1V 0A6, Québec, Canada. Email: david.conciatori@gci.ulaval.ca

[5] Associate Professor, Department of Construction Engineering, École de Technologie Supérieure, 1100 rue Notre-Dame Ouest, H3C1K3, Montréal, Canada. Email: claudiane.ouellet-plamondon@etsmtl.ca

Abstract

The use of locally available industrial by-products as supplementary cementitious materials and mineral fillers is vital for reducing the embodied carbon of modern concretes. Spent pot lining (SPL) is a by-product of the aluminum industry, which is massively produced worldwide. SPL treated by the Low Caustic Leaching and Liming process (called LCLL-ash) is not any more hazardous and can be used as cementitious materials. This study aims to better understand the microstructure changes of cement paste incorporating aluminum smelter wastes, such as LCLL-ash and synthetic anhydrite. Ground LCLL-ash was used to partially replace cement in cement pastes with a constant water-to-binder ratio of 0.35. A small amount of anhydrite was added to some mixes. This study investigated chemo-micromechanical properties of cement paste systems by a multiple-technique approach, including X-ray diffraction, thermogravimetric analysis, scanning electron microscopy, wavelength-dispersive spectroscopy, and microindentation test. The results showed the reactive alumina from LCLL-ash modified the hydrated phases with the presence of the carbo-aluminate phases. The pastes containing LCLL-ash exhibited a higher CH, and C-S-H contents refer to the

reference, suggesting that LCLL-ash has a slight nucleation effect. Moreover, LCLL-cement paste showed an increase in the Ca/Si ratio of the C-S-H phase intermix. Finally, microindentation results revealed that adding anhydrite with 10% LCLL-ash enhanced the mechanical property of the cement paste at 28 days.

Author keywords: Portland cement paste; Treated refractory spent lining; Filler; Microstructure; Cement Hydration; Hydrated phases; Microindentation.

Introduction

The use of industrial by-products as supplementary cementitious materials (SCM) or mineral fillers to reduce the cement content in concrete is a promising strategy to reduce its critical contribution to worldwide carbon emissions (Poudyal and Adhikari, 2021; Scrivener, 2014). In particular, the recycling of industrial by-products which are locally available allows for reducing the environmental impact of transport (Khatri et al., 1995).

Several SCMs, such as silica fumes, fly ashes, and ground blast-furnace slag, have been employed to recycle industrial by-products by replacing up to more than 50% of cement content (Feng et al., 2013; Haha et al., 2010; Kocaba et al., 2012; Scrivener et al., 2017). In general, SCMs improve not only the ecological imprints of concrete but can also enhance its durability, e.g., mitigating the risk of alkali-reaction or preventing water absorption (Aghamohammadi et al., 2022; Amran et al., 2021; Saha et al., 2018; Scrivener et al., 2017). However, the performance of concretes containing SCMs is affected by many factors, such as their chemical composition mineralogical and physical properties (Adesina and Das, 2020; de Grazia et al., 2021; Faried et al., 2021). One of the major limitations to the use of SCM is the transport cost, and thus, the development of new sources which are locally available is of great interest today. As an example, glass powder recycled from the post-consumed glass is today used as supplementary cementitious material in concrete (Wilson et al., 2018a). Furthermore, industrial by-products can act as mineral fillers and are efficiently employed to favor cement hydration and develop concretes with a low water-to-cement ratio (Camiletti et al., 2013; Mindess, 2019).

Spent pot lining (SPL) is a hazardous industrial waste from the primary aluminum industry after 5-8 years of operation (Birry et al., 2016; Broek, S., Øye, H.A., 2018). It is considered that each ton of aluminum product generated about 22 kg of SPL. In 2018, producing 64 million tonnes of primary aluminum generated approximately 1.4 million tonnes of SPL (Holywell and Breault, 2013). Roughly 80000 tonnes of SPL is produced in Canada per year, with about 35000 tonnes coming from Rio Tinto (Birry et al., 2016). Demand for aluminum is expected to grow significantly by 2040 ("International Aluminium Institute. Global Mass Flow Mode," 2018). This means that it will also lead to increased SPL generation. However, it is not possible to landfill SPL due to the high levels of leachable cyanides and fluorides, but also to its hydro reactivity creating explosive gases (Rustad et al., 2000). SPL is made of two parts: (i) the 1st cut is rich in carbonaceous materials; (ii) the 2nd cut is rich in vitrified refractory. The chemical composition of SPL first and second cut is about 30±5% of carbon, 15 ± 3% of fluoride, 15 ± 3% sodium, 15 ± 3% aluminum and a minor amount of sulfur and calcium ("The SPL Waste Management Challenge in Primary Aluminum," 2021). It is possible to utilize SPL without treatment as a raw material at a cement plant or as an additive in steelmaking is the most common as done in Europe, China, Brazil, Russia and South Africa (Al-Maqbali et al., 2016; Øye, 2017). The carbon part has caloric value and can be used as a fuel substitute mixed with coal. The fluoride content reduces fuel consumption by up to 4% (Broek, S., Øye, H.A., 2018). The utilization of SPL in the cement industry provides a saving in fuel as it offers the solution to ecological problems created by the disposal of SPL waste (Øye, 2017). However, the replacement of raw meal by SPL must be limited to 0.2%-0.75% to avoid durability concerns of concrete caused by the alkalis-silica reactions (Fernandes and Broekmans, 2013; Gomes et al., 2016). This practice is currently not allowed in the North American cement industry due to the high percentage of fluoride in SPL.

Developed in early 2000, a thermal treatment (pyro-metallurgical process) allowed to obtain Glass Frit (GF) (Laldji and Tagnit-Hamou, 2007). This by-product showed a reactivity behavior similar to slag (Fares, 2008; Laldji and Tagnit-Hamou, 2007). In addition, Laldji et al .(Laldji et al., 2010) showed that GF exhibited better durability with a low chloride ion permeability, excellent resistance to freezing-thawing and improved resistance to the alkali-silica reaction. SPL can be also treated by a hydro-metallurgical

process called “Low Caustic Leaching and Liming” (LCL&L), developed by Rio Tinto in the early 1990s, to extract toxic elements, including leachable cyanides and fluorides (Birry et al., 2016). The first step of this process is to grind the SPL to a size smaller than 300 µm by an air-swept autogenous mill. Then the first leaching step is done with water to extract the water-soluble fluorides and cyanide compounds, followed by a low caustic leach to extract the remaining fluorides and cyanides. Carbon and insoluble are filtered out. The liquor after cyanide destruction in a pressurized reactors by high temperature (hydrolysis (180° C) is concentrated by evaporation and NaF is precipitated out. Finally, the sodium ion concentration is reduced significantly, and the fluorides and cyanides are extracted. Treated SPL is an inert by-product with a limited amount of Na and F content than untreated SPL with a high potential for valorization (Kimmerle et al., 2001). By treating only refractory bricks (2^{nd} cut) separately from the carbon part (1^{st} cut), an industrial by-product herein called LCLL-ash is produced. LCLL-ash has a grey color, mainly composed of oxides of silicon and aluminum, with minor fractions of sodium, iron, and sodium oxides. About 20 kt of LCLL-ash is produced every year in Quebec. Very recently, Brial et al. (Brial et al., 2021a) studied the reactivity of LCLL-ash as supplementary cementitious materials by using the Rilem R^3 pozzolanic test. The results showed that the LCLL-ash acts as an inert addition similar to quartz powder due to the presence of silicate phases, such as albite and/or nepheline. Interestingly, due to the high amount of reactive alumina in calcinated LCLL-ash, new hydrated phases may precipitate, such as carbo-aluminate phases. However, the presence of phases containing alumina leads to hydro-reactivity (gas expansion), which is a complex phenomenon dependent on many factors, such as temperature, chemistry, and pH. In addition, this study is limited to solution reactivity tests and compression tests on standardized mortar with only 20% cement replacement by LCLL-ash.

Moreover, synthetic anhydrite ($CaSO_4$) is another solid industrial by-product of aluminum smelters. For instance, it is produced by a fluoride plant by using BUSS technology in Quebec. Aluminum fluoride is an important additive for aluminum smelters. In particular, anhydrite is produced in the gasifier, where the spat fluor (CaF_2) and sulfuric acid (H_2SO_4) react to produce hydrofluoric acid. At the gasifier exit, synthetic

anhydrite is neutralized with lime. Synthetic anhydrite consists of more than 95% $CaSO_4$ and other trace elements. About 80-110 kt of anhydrite is produced per year. This product is valorized in several applications, such as drying agent, as raw material instead of gypsum ($CaSO_4*nH_2O$) for cement plants, for floor screed (self-leveling) and as fertilizer for agriculture.

To the authors' knowledge, there is no data available in the open literature on the effect of LCLL-ash on the microstructure features of a cement paste. Also, fostering the recent work on the reactivity of LCLL-ash by Brial et al. (Brial et al., 2021a), this work aims to investigate and better understand the effect of replacing cement with LCLL-ash on the chemo-micromechanical properties of a cement paste using multiple techniques. In particular, this study investigated different replacements of cement up to 20% by LCLL-ash. Furthermore, the addition of a small amount of synthetic anhydrite by-products is also investigated.

Research significance

Driven by the urgency of fighting climate changes, concrete industries, and renewable energy solutions by 2030-2050 will imply a significant reduction of available quantities of SCMs for concrete (Environment et al., 2018). For example, the coal plants in Canada will no longer be used by 2030 (Canada, 2017), and concrete producers want to use more fly ash in concrete (Adams, 2020), resulting in the scarcity of fly ash. Considering that the worldwide use of concrete is increasing due to population growth, there is a strategic need to seek alternative sources of SCM or mineral fillers. The partial replacement of cement with the aluminum by-products will contribute to an effective circular economy solution for countries with a major aluminum production, such as China, Europe, Asia, North America and Latin America. Moreover, developing locally available LCLL-cement will reduce landfilling aluminum waste and the cost of concrete.

Materials and methods

Materials

A commercially ordinary Portland cement (OPC) type GU with estimated Bogue phase composition of 51.2% C_3S, 16.2% C_2S, 6.7% C_3A, 11.0% C_4AF and a Na_2O of 0.25% was used. LCLL-ash and synthetic anhydrite were supplied by an aluminum production. LCLL-ash was dried and grinded by means of the

laboratory vibrating cup mill (type Pulverized 9) at a speed of 1000 rpm for 2 minutes and 30 seconds. The particle size distribution (PSD) was measured by Mastersizer 2000 laser diffraction spectrometry of a dilute particle suspension in isopropyl alcohol. Fig. 1 shows the particle size distribution of LCLL-ash and cement. Fig. 2 illustrates the SEM micrographs of cement, LCLL-ash and anhydrite. While irregular shapes and sharp edges characterize the particles of cement and LCLL-ash, anhydrite grains are quite spherical. The chemical composition of LCLL-ash, and cement were determined by X-ray fluorescence spectrometer (ZSX Primus II). The specific surface area of LCLL-ash was measured by BET method using Micromeritics Tri STAR II. Table 1 shows the chemical and physical properties of LCLL-ash, and cement, respectively. The compositions of LCLL-ash are mainly SiO_2, Al_2O_3 and Fe_2O_3. A high content of alkali content can be found in LCLL-ash, which is approximately 8% in weight of sodium oxide. Fig. 3 shows the X-ray diffraction analysis of LCLL-ash measured by X-ray diffraction (PANanlytical). LCLL-ash is mainly composed of crystalline phases such as corundum, nepheline, albite, anorthite and some amount of graphite (Brial et al., 2021b). The AH granulometry was not investigated as it rapidly reacts with water.

Mix formulation and curing

Table 1 summarizes the mix-design series with different cement replacement percentages at 0%, 10% and 20% by weight (wt.) with LCLL-ash. A small amount of synthetic anhydrite (AH) was also added in some mix-design (1.25 % and 2.5 % by wt. of cement). The material code corresponds to the percentage of cement replacement by LCLL-ash and anhydrite (Table 1). The cement pastes samples prepared with a water-to-binder ratio (*w/b*) of 0.35 were poured into cylindrical specimens of 25 mm in diameter and 150 mm in height. After 24 h at room temperature, the specimens were demolded and cured in saturated limewater at an environmental temperature of 20°C ± 3°C with 55% relative humidity. The hydration of the specimen was stopped at the desired ages by immersing them in isopropanol (1:1 by volume) for 7 days. According to the previous results (Thomas, 1989), isopropanol exchange was employed to stop hydration for investigating the microstructure phase assemblage. Subsequently, the samples were conserved in a desiccator with soda lime to prevent carbonation for the analysis.

152 ***Experimental Tests and Methods***

153 **X-ray diffraction**

154 X-ray diffraction (XRD) was employed to observe the formation of crystalline hydrates and non-reacted
155 raw materials in hardened pastes on different curing days. XRD analysis was performed using Philips
156 X'pert APD operating at a tube voltage of 40 kV, a tube current of 40 mA, and Cu K∝ radiation. About 3g
157 of hydrated paste was crushed and finely ground using a mortar and a pestle. Then, the sample should be
158 immersed in 100 mL of isopropanol immediately after crushing for 10 min. The ground powders were dried
159 for 10 min in a ventilated oven at 40 ± 5 °C. The analyses were performed within an angle range of 5-70°
160 2 theta. The step width was set at 0.02, and the scan rate was 2°/min.

161 **Thermogravimetric analysis**

162 Thermogravimetric analysis (TGA) (Netzch STA 449 F3 Jupiter) was used to measure the mass loss upon
163 heating the sample. For each test, about 40 mg of powder were taken in a ceramic crucible without lid. The
164 heating ramp varied between 50 °C and 950 °C with a heating rate of 20°C/min. The test was done under a
165 nitrogen atmosphere at a flow rate of 50 mL/min.

166 Following previous studies, the amount of CH and C-S-H can be estimated from the TG curve using the
167 tangential method (Scrivener et al., 2016). The measured content of CH and C-S-H are expressed as
168 percentage of the dry sample weight at 500 °C as the following equations (Wei et al., 2016):

169 $$CH = \frac{W_{400} - W_{500}}{W_{500}} \text{x} \frac{M_{CH}}{M_{H_2O}} \quad (1)$$

170 $$C-S-H = \frac{W_{150} - W_{400}}{W_{400}} \text{x} \frac{M_{C-S-H}}{2.1 M_{H_2O}} \quad (2)$$

171 where W_T is the dry sample weight at the temperature T (°C) (400-500 °C for CH and 150-400 °C which
172 should exclude AFm peak (Scrivener et al., 2016)), M_{CH} , M_{C-S-H} and M_H are the molecular weight of
173 CH, C-S-H gel, and water, respectively. The chemical formula of C-S-H is taken as $C_{1.7}$ SH_4, some part of
174 the 4 moles of water has already been lost below 150 °C (Jain and Neithalath, 2009). The equilibrium

composition of C–S–H is thus taken as $C_{1.7}$ $SH_{2.1}$ as given in (Taylor, 1997), which explains the division by 2.1 used in in Eq. (2).

Scanning Electron Microscopy

Scanning electron microscopy (SEM) was carried out to study the microstructure of the blended cement pastes. The employed Scanning electron microscopy (SEM) instrument was the commercial brand Tescan Vega3. The samples were cut into 3 mm thick slices by a diamond saw. The slice was then impregnated with low viscosity epoxy under a vacuum. The impregnated sample was cured at 40°C for 24 h. The specimens were glued on metallic discs and polished with Anamet perforated polishing cloths installed on Ultrapol automatic polishing machine, applying an oil-based diamond suspension of different particle size (6 µm and 1 µm) for 1 h each. Before testing, the sample was coated with carbon to avoid electrical charges on the surface sample.

Wavelength Dispersion Spectroscopy

The electron probe micro-analyzer is a microbeam equipped with wavelength dispersive spectrometers (WDS). WDS is to characterize materials based on X-rays emitted from the solicited specimen because of interaction between the sample being analyzed and an electron beam. WDS analysis classifies emitted X-rays based on their wavelengths and offers spatial resolutions on the micrometer range depending on the electron beam energy and sample density (Goldstein et al., 2003). It is worthy to note that WDS is a quantitative technique to measure chemical elements within a probed material spot. WDS is calibrated with mineral standards and the detection limits of WDS provide quantitative analyses in the 50–100ppm range (0.005–0.01wt%, elemental) with an accuracy and precision on the order of 1% (Reed, 2005). To avoid charging during high-vacuum chamber, the samples were coated with a thin layer of carbon. The WDS was measured by using a EPMA Cameca SX-100. The polished sections (the same sample preparation for SEM) were examined at an accelerating voltage of 15 kV and a dwell time of 0.04 seconds. The beam size is approximately 1 to 2 µm, based on previous work of (Vanzo, 2010). The grid of 20x20 points spaced by 3 µm were performed.

200 **Microindentation test**

201 For the sample preparation, the sample surface was cut into an ideal size of 25 mm in diameter and 5 mm
202 in thickness at the middle portion. The surface was polished by using the same machine in section 2.3.3,
203 according to a well-established procedure (Frech-Baronet et al., 2017; Vandamme and Ulm, 2013; Wei et
204 al., 2017), such as: (i-iv) the coarse polishing using different grit sizes (400, 600, 800 then 1200) was
205 employed during 15 min for each paper; (v-vi) after that, oil-based diamond suspension (6 μm and 1 μm)
206 were used during 15 min and 30 min, respectively. Between each polishing step, specimens were cleaned
207 with isopropanol for 3 min in an ultrasonic bath to remove any debris.

208 For the microindentation test, the penetration depth h_{max} should be chosen to be large enough to assure a
209 homogenous response while considering that the probed volume is about 5-10 times of h_{max} (Ulm et al.,
210 2010, 2007). In this study, the maximum applied load is 10 N, and the holding force is 300 seconds before
211 unloading for creep investigation. A matrix of 10 x 10 indents was performed on each sample with an inter-
212 distance of 500 μm (to avoid interaction between indented areas). The indentation tests were carried out by
213 using a MCT CSM Instruments Indentation Tester. The indentation method consists of applying a load to
214 the surface of the sample with a rigid indenter, typically a Berkovich diamond, with different phases: (i)
215 loading phase; (ii) holding phase at constant load; (iii) unloading phases. The indentation modulus (M) and
216 the contact area A_c needed to estimate the indentation hardness (H) are estimated by the initial slope of the
217 load (P) vs. penetration depth (h) curve in the unloading branch (Fig. 4). Based on continuum mechanics
218 analysis of the P-h curve (Miller et al., 2008), the indentation properties (H and M) are defined by the
219 following relations:

220
$$H \overset{def}{=} \frac{P_{\max}}{A_c} \tag{3}$$

221
$$M \overset{def}{=} \beta \frac{\sqrt{\pi}}{2} \frac{S}{\sqrt{A_c}} \tag{4}$$

where P_{max} is the maximum load applied; A_c is the projected area of the indenter; and $S = (dP/dh)_{h=hmax}$ is the initial slope of the unloading branch of the P-h curve; β is a coefficient accounting for the slip on the indenter surface and can be extrapolated from the indentation depth h using the Oliver and Pharr method (Oliver and Pharr, 1992).

One of the major advantage of microindentation is rapidly measuring the logarithmic basic creep of a cement paste (Frech-Baronet et al., 2017; Vandamme and Ulm, 2013). For modeling indentation creep of cementitious materials, Vandamme et al. (Vandamme and Ulm, 2013) proposed the logarithmic contact creep compliance equation as :

$$L(t) = \frac{1}{M(t)} = \frac{1}{M_0} + \frac{1}{C}\ln\left(1 + \frac{t}{\tau}\right) \quad (5)$$

where C is the contact creep modulus C and τ is the characteristic time. The contact creep modulus (C) is further defined as follows (Vandamme, 2008; Wei et al., 2017):

$$C = \frac{P_{\max}}{2x_1\sqrt{A_c/\pi}} \quad (6)$$

where x_1 can be estimated by fitting the increase of indentation depth Δh(t) under constant loading by $\Delta h(t) = x_1 \ln\left(x_2 t + 1\right)$.The contact creep modulus C is today widely employed to measure the logarithmic creep rate of a cement paste and can be reasonably used to predict the long-term deflection of structures (Baronet et al., 2021).

Results and discussion

Hydration products by XRD

XRD allows a qualitative identification of the different crystalline phases composing the cement paste microstructure. Fig. 5 shows the XRD patterns of hardened cement pastes with and without LCLL-ash at 28 days. The main hydration products were ettringite (AFt) and portlandite in addition to mineral components such as unreacted clinker phases and unreacted LCLL-ash. The pattern of ettringite and ferrite is visible for all tested samples at 9.1° 2θ and 12.2° 2θ, respectively. Moreover, anhydrite addition systems

(10LCLL-1.25AH and 20LCLL-2.5AH) show a broader ettringite peak. This is attributed to a quickly dissolving of calcium sulfate, which then reacts with calcium aluminates during the early hydration to form more ettringite (Soroka and Abayneh, 1986; Zajac et al., 2014). The main LCLL-ash crystalline phases, such as sodium aluminate oxide ($NaAlO_2$) at 7.9° 2θ and quartz at 26.4° 2θ, are still clearly present in all OPC-LCLL-ash blended cement pastes, particularly in samples that have higher contents of LCLL-ash in the mixture.

Fig. 6 shows the XRD patterns of hydrated cement pastes at different curing days. As observed in samples with 10 % and 20% substitution, the formation of AFm phase assigned as hemicarbonate peak (that is, calcium hemicarboaluminate hydrate, Hc) is detected at 7 days and 14 days, respectively, but it seems to level off after 14 days, whereas the monocarbonate peak (that is, calcium monocarbonaluminate hydrate, Mc) grows over time until 112 days. More interestingly, the intensity of Mc peak increases with the increase of LCLL-ash content (10LCLL and 20LCLL). This can explain by two possibilities: (i) owing to the reactive alumina from LCLL-ash and calcite in the binder to form Mc (Feng et al., 2015; Matschei et al., 2007; Zajac et al., 2014); (ii) AFm is mainly formed by the reaction of CO_2 with CAH, similar phenomena of hydration of metakaolin-cement (Antoni et al., 2012). The ferrite phase was identified over 112 days in this study.

Hydrate content by TGA

TGA analysis aims at estimating the content of Portlandite and C-S-H of the cement pastes. Fig. 7 shows thermogravimetric curves of hydrated cement paste samples at 7 and 28 days of hydration. Derivative thermogravimetric (DTA/DTG) curves were also plotted from TG data to identify the exact boundaries of phases presented in the hydrated sample. Four endothermic phases are observed. The first one is related to the evaporation of absorbed surface moisture in the range of 30- 110 °C. The second observed range is 110-400 °C showing the dehydration of calcium aluminate hydrate and calcium silicate hydrate. The hydrates decomposition, between 400 and 500 °C, corresponds to the CH dehydration during hydration. The final range corresponds to the decarbonation of calcium carbonate (600-800 °C). It is noted that the intensity of

the first peak is more pronounced for 10LCLL-1.25AH and 20LCLL-2.5AH systems. Therefore, it is possible to assign these peaks to the presence of ettringite and AFm phases. These phases are formed by adding sulfate in anhydrite or reactive alumina in LCLL-ash, which corroborates data of XRD results.

Fig. 8 shows the estimated content of C-S-H and CH at 7 days and 28 days, respectively, in terms of the total mass and mass normalized to the cement mass. As for the cement paste (control sample), the C-S-H and CH contents increase over time due to C_3S and C_2S hydration as expected. As for the cement pastes with LCLL-ash in Fig. 8a, C-S-H content at 7 days in the control sample is lower than that of the paste containing LCLL-ash, i.e., the C-S-H increase from 38.5% to 51.0% by mass of cement by adding 20% of LCLL-ash, which is an increase of about 32%. This can be attributed to different possible reasons, such as (i) the nucleation effect of LCLL-ash particles, (ii) increases the water-to-cement resulting in having more space for hydrating of cement; (iii) the formation of other hydrates phases, such as carbo-aluminate (e.g., Hc and Mc) and AFt might have been included in the estimated content of C-S-H as difficult to separate their thermo-gravimetric effects. At a later hydration stage (28 days in Fig. 8d), the increase of the amount of C-S-H by mass of cement due to LCLL-ash addition is about 21% (i.e., the C-S-H increase from 48% to 58% by mass of cement by adding 20% of LCLL-ash), which is less important than the gain at 7 days.

The CH contents in OPC-LCLL-ash systems reduce with the increase of LCLL-ash content at both 7 days and 28 days, as shown in Fig. 8b and Fig. 8d. Note that the amount of CH content by mass of cement in OPC-LCLL-ash systems at 28 days is lower than that of control paste due to the lower content of cement (Table 2). The fact that CH reduces by adding LCLL-ash may indicate that the reason for the aforementioned increase of C-S-H content is due to additional rich-aluminate hydrates.

Microstructure texture by SEM

Fig. 9 shows SEM micrographs of the hardened pastes at 28 days. The microstructure of cement paste with LCLL-ash particles appears different from that of the control sample, which shows a denser morphology. This can be explained by the filler effect of LCLL-ash particles during the hydration of cement (Bentz, 2005; Bentz et al., 2009). However, 20LCLL shows to be more porous than the control, which is perhaps

due to the dilution effect. The few micro-crack observed are likely due to dehydration under vacuum or autogenous shrinkage (Lura et al., 2009). Furthermore, both unreacted clinkers and unreacted LCLL-ash particles are still visibly embedded in the cement paste matrix Fig. 9b and 9c.

Phase distribution by WDS chemical analysis

This analysis aims to quantify the phase distribution and microstructure heterogeneity better. In particular, the WDS quantitative analysis was performed on the control and 10LCLL samples to understand the effect of LCLL-ash particles on the chemical properties of the blended cement paste. Fig. 10 shows the WDS spot contour of the 10LCLL sample at 28 days. As an observation, the areas with a high level of Ca and Si are residual clinker. The LCLL-ash particles are rather heterogeneous in elemental compounds and non-uniform sizes. For example, the particle with a high concentration of Al, Na, Si, and O on the mapping can be associated with albite, accounting for about 20% of LCLL-ash (Brial et al., 2021a). Fig. 10 shows that very fine LCLL-ash particles of micrometer dimension can be found dispersed in the cement paste matrix.

Fig. 11 presents the chemical clustering with 5 quantitative chemistry variables (Si/Ca, (Fe+Al)/Ca, s/Ca, Mg/Ca, Sum of Oxides (SOX). The cluster deconvolution analysis was carried out by a statistical most-likelihood algorithm which was used in previous work (Wilson et al., 2018a, 2018b). Such method was applied in several previous works and allows for to identify of the phases with a similar chemical structure by most-likelihood estimation of the aforementioned 5 quantitative chemistry variables (Wilson et al., 2018b). That is, the identified cluster is a statistically recognizable phase or intermix of different phases.

The microstructure of a hydrated OPC cement is highly heterogeneous and made of a complex intermix of several hydrated phases such as C-S-H, CH, AFt, as well as residual clinkers (Scrivener et al., 1986; Scrivener and Pratt, 1984; Wilson et al., 2018b). Table 3 and Table 4 present the estimated 6 clusters for OPC and 7 clusters for 10LCLL, respectively. In this section, we have used the vocabulary of previous works by Wilson (Wilson et al., 2018b) to describe the intermix phases which may compose a cluster, such as: (i) cluster #1 is Al-rich clinker (C_4AF, C_3A) intermix with C-S-H; (ii) cluster #2 is CH intermix with C-S-H; (iii) cluster #3 is AFt intermix with C-S-H; (iv) cluster #4 is a very small fraction of silicate clinkers

(alite and belite); (v) cluster #5 «Others» is a minor phase which is not identified; (vi) cluster #6 is mostly C-S-H; (vii) cluster #7 is a intermix with mostly LCLL-ash particles.

As for neat paste microstructure, only cluster #6 can be considered as a mostly pure phase made of C-S-H, which has similar results to the referenced work (Wilson et al., 2018b). The cluster #3 «Al-rich + C-S-H» has more content in LCLL-ash system due to the formation of monocarboaluminate Mc products of which presence is confirmed by XRD results.

Fig. 11 graphically plots the estimated clusters in terms of chemical mass ratios (Fe+Al)/Ca vs. Si/Ca (a-1, b-1), (Na+Al)/Ca vs. Si/Ca (a-2, b-2), Si/Ca vs. sum of oxides (a-3, b-3) for the 2 systems (control and 10LCLL). Clinker phases should have a sum of oxide equal to 1, while a sum of oxide of theoretical C-S-H is close to 0.7. It can be seen that the C-S-H phase (cluster #6) did not increase its aluminate content (Fig. 11a-1 vs. b-1), which confirms that confirming no aluminum uptake by C-S-H (L'Hôpital et al., 2016). However, the Ca/Si ratio of cluster #6 (mostly C-S-H) with 10LCLL system (1.72) is higher than that for the control system (1.53). The Ca/Si ratio is an important parameter of the C-S-H structure, but this shift is too small to evoke a C-S-H phase change (Alizadeh, 2009; Shahsavari et al., 2009; Sorelli et al., 2012). In addition, unreacted LCLL (cluster #7) can be found in LCLL-ash system. Fig. 11(b-3) shows the very high Si/Ca ratio of cluster #7 as LCLL-ash is rich in Si and low in Ca content (Table 1). Notably, the C-S-H cluster #6 has similar values of (Fe+Al)/Ca for OPC and LCLL-ash systems (a-1 vs b-1), which also hints that there was no aluminate uptake from C-S-H and no formation of C-A-S-H for such system.

Micromechanical properties by micro-indentation

Fig. 12 shows the micro-indentation results of hardened pastes of control and OPC with different amounts of LCLL-ash at 28 days, 56 days, 112 days of hydration. While the contact creep modulus (C) describes the logarithmic rate of the basic creep of a cement paste (Frech-Baronet et al., 2017; Vandamme, 2008), the indentation modulus (M) and indentation hardness (H) are related to the elastic modulus and the compressive strength of a cement pastes, respectively (Bobko et al., 2011; Fischer-Cripps, 2004; Zhang et al., 2014). To make sure that the variation of micro indentation property is statistically acceptable, an

analysis of variances (ANOVA) was carried out. Table 5 reports the results at different curing days, P-value with the normal distribution and the F-test with the Fisher—Snedecor distribution. These results are verified as P is much lower than the threshold $\alpha = 0.05$, while F is much greater than F_{crit}. Therefore, the observed effect of LCLL-ash on the indentation properties M and H is meaningful and statistically acceptable.

As observed in Fig. 12, the mechanical properties of the control sample increase with the hydration time due to the formation of hydration products, mainly C-S-H, and the reduction of porosity (Diamond, 2004). For OPC-LCLL-ash samples, the same trend was also observed. The indentation properties of the 10LCLL sample (90% OPC+ 10% LCLL-ash) are comparable with those of control sample. In the case of the 20LCLL sample, the micro-indentation properties are slightly reduced with respect to other systems. Compared to control, the indentation hardness H of 20LCLL sample at 28 days, 56 days and 112 days was reduced by 1.29, 1.15 and 1.10, respectively. As we have carried out the comparison of systems with the same water-to-binder ratio, this decrease may be attributed to the reduction of the water-to-cement (w/c) ratio. The w/c ratio was passing from 0.35 to 0.43 for the control to 20LCLL, which might have caused a more porous cement paste with negative effect on the strength (Talero et al., 2017). Based on previous work of microindentation of cement paste (Bobko et al., 2011; Cariou et al., 2008), the increase of Hardness is due to an increase in the property of friction and cohesion of the material, which increases the compressive strength. The creep compliance C is a powerful indicator of the basic creep of the cement paste as it correlates very well with the logarithmic creep compliance measured by macroscopic compressive creep tests over 1 year time as shown by several works published in the open literature (Frech-Baronet et al., 2017; Vandamme, 2008). The more the concrete creep compliance, the lower the concrete creep.

Fig. 12 compares the H, M and C, respectively, for all the systems at different ages in terms of percentage variation with respect to the reference system. The mix-designs incorporating LCLL-ash and anhydrite (10LCLL-1.25AH and 20LCLL-2.5AH) showed higher values of H and contact creep modulus C, compared to the reference samples at 28 days. Notably, the results of microindentation confirm the TGA results. Indeed, the sample 10LCLL-1.25AH, characterized the highest amount of hydration products C-S-

H at 28 days, also has the highest hardness H and highest creep modulus C. The possible reason is the increase of ettringite (AFt) due to adding anhydrite (AH), which might have strengthened the cement paste microstructure. The increase in the content of ettringite was also confirmed by XRD (Fig. 5). According to the results of Zajac et al. (Zajac et al., 2014), the formation of ettringite increased concrete strength at early ages (less than 2 days), but the results from this search found that the addition of sulfate improved the strength of cement paste strength at later age of 28 days.

At later stage, the enhancement of H and C of the systems with anhydrite was less important at 56 days with respect to the cement paste and even disappeared at 112 days (Fig. 12 a.1, b.1 and c.1). This may be attributed to the hydration process of cement in the reference sample, which increased the hydrates product, resulting in a denser matrix.

Conclusions

This study investigates the microstructure changes of cement pastes with cement partially replaced by two industrial by-products of Aluminum smelters, such as LCLL-ash and synthetic anhydrite. Based on the presented results, the following conclusions can be drawn:

1. Based on XRD results, the cement pastes with LCLL-ash contains new hydrates products such as the hermicarboaluminate Hc at 7 days, which transforms into monocarbonaluminate Mc at 28 days. The latter appears chemically stable at 112 days, as proven by XRD patterns. The ettringite peaks in cement pastes with LCLL-ash and anhydrite is more marked than in other systems. Moreover, unreacted LCLL-ash particles are visible;
2. Based on TG/DTA results, the addition of LCLL-ash increases the C-S-H content due to a filler effect or the formation of aluminate-rich phases among C-S-H hydrates (e.g., Hc, Mc and AFt), which was observed by XRD;
3. Based on BSE images observation, the microstructure of hardened cement paste containing 10% LCLL-ash appeared denser than the one of the neat paste. The unreacted LCLL-ash particles were visible, and they seem to act as a filler inclusion embedded in the matrix of hydrated products;

4. Based on WDS analysis and statistical clustering analysis of the cement paste with 10% LCLL-ash, the C-S-H predominant phase did not increase its aluminate content, which confirms that there is no aluminum uptake. However, a slight shift of the Ca/Si ratio was observed, which may cause a change in the silicate chain length. This suggests that the tiny LCLL-ash particles are intimately intermixed with C-S-H gel;
5. Based on microindentation results, the mechanical properties of the cement paste at different ages were not weakened by replacing with 10% of cement by LCLL-ash. Moreover, the cement paste with anhydrite (AH) and LCLL-ash exhibited greater hardness H and creep compliance C at 28 days. The addition of AH led to an increase in the volume of hydrates (most likely ettringite) with a gain in strength.

As a concluding remark, the cement paste with a cement replacement of 10% by LCLL-ash is a promising research direction for developing sustainable concrete recycling industrial by-products from aluminum smelters, but further works are needed before a possible commercialization. Considering the high alkali content (8.2wt%) of LCLL-ash, further investigation on the risk of Alkali Silica Reaction (ASR) shall be carried out. It may be possible that the small size of LCLL-ash particle mitigate such a risk as for glass admixture (Vijayakumar et al., 2013). Furthermore, the analysis of the highly heterogeneous microstructure phases might require advanced chemo-mechanical techniques (Wilson et al., 2018b, 2018a). Finally, Life Cycle Analysis (LCA) should be carried out for assessing the environmental benefit of specific applications of LCLL-ash.

Data Availability Statement

Some or all data, models, or code that support the findings of this study are available from the corresponding author upon reasonable request.

Acknowledgments

The research discussed herein was funded by the NSERC CRD grant program (CRDPJ 515485 – 17) and the CRITM consortium. In addition, the authors would like to thank Professor Wilson for the MATLAB

algorithm to do the statistical clustering analysis and his advice for the results of WDS. We also would like to thank Rio Tinto and Cement Quebec Inc. for financing this industrial project. We finally would like to acknowledge Mr. Laurent Birry from Rio Tinto and Mr. Martin Beaulieu of Cement Quebec for their expert advice during the project.

References

Adams, T.H., 2020. Fly Ash Use in Concrete Increases Slightly As Overall Coal Ash Recycling Rate Declines 5.

Adesina, A., Das, S., 2020. Influence of glass powder on the durability properties of engineered cementitious composites. Construction and Building Materials 242, 118199.

Aghamohammadi, O., Mostofinejad, D., Abtahi, S.M., 2022. Effects of Surface Modification of Crumb Rubber with Polyvinyl Acetate on Rubberized Concrete. MJ 119, 195–206. https://doi.org/10.14359/51734195

Alizadeh, R.A., 2009. Nanostructure and engineering properties of basic and modified calcium-silicate-hydrate systems. University of Ottawa (Canada).

Al-Maqbali, A., Feroz, S., Ram, G., Al-Dhamri, H., 2016. Feasibility Study on Spent Pot Lining (SPL) as Raw Material in Cement Manufacture Process 10.

Amran, M., Fediuk, R., Gunasekaran, M., Vatin, N., Karelina, M., Ozbakkaloglu, T., Krishna, R.S., Kumar, A., Das, S., Mishra, J., 2021. Rice Husk Ash-Based Concrete Composites: A Critical Review of Their Properties and Applications. Crystals 11, 168. https://doi.org/10.3390/cryst11020168

Antoni, M., Rossen, J., Martirena, F., Scrivener, K., 2012. Cement substitution by a combination of metakaolin and limestone. Cement and Concrete Research 42, 1579–1589. https://doi.org/10/ghdfsw

Baronet, J., Sorelli, L., Charron, J.-P., Vandamme, M., Sanahuja, J., 2021. A two-time-scale method to quickly characterize the logarithmic basic creep of concrete by combining microindentation and Uniaxial Compression Creep Tests. Cement and Concrete Composites.

Bentz, D.P., 2005. Replacement of "coarse" cement particles by inert fillers in low w/c ratio concretes: II. Experimental validation. Cement and Concrete Research 35, 185–188.

Bentz, D.P., Irassar, E.F., Bucher, B.E., Weiss, W.J., 2009. Limestone fillers conserve cement; Part 1: an analysis based on Powers' model. Concrete international 31, 41–46.

Birry, L., Leclerc, S., Poirier, S., 2016. The LCL&L Process: A Sustainable Solution for the Treatment and Recycling of Spent Potlining, in: Williams, E. (Ed.), Light Metals 2016. Springer International Publishing, Cham, pp. 467–471. https://doi.org/10.1007/978-3-319-48251-4_77

Bobko, C.P., Gathier, B., Ortega, J.A., Ulm, F.-J., Borges, L., Abousleiman, Y.N., 2011. The nanogranular origin of friction and cohesion in shale—a strength homogenization approach to interpretation of nanoindentation results. International Journal for Numerical and Analytical Methods in Geomechanics 35, 1854–1876.

Brial, V., Tran, H., Ouellet-Plamondon, C., Sorelli, L., Conciatori, D., 2021a. Evaluation of the reactivity of treated spent pot lining from primary aluminum production as cementitious materials. Resources, Conservation & Recycling.

Brial, V., Tran, H., Sorelli, L., Conciatori, D., Ouellet-Plamondon, C.M., 2021b. Evaluation of the reactivity of treated spent pot lining from primary aluminum production as cementitious materials. Resources, Conservation and Recycling 170, 105584. https://doi.org/10.1016/j.resconrec.2021.105584

Broek, S., Øye, H.A., 2018. Fundamentals of Managing Spent Potlining (SPL). Trav. 46, Proc. 585 35th Int. 817-834.

464 Camiletti, J., Soliman, A.M., Nehdi, M.L., 2013. Effect of nano-calcium carbonate on early-age properties
465 of ultra-high-performance concrete. Magazine of Concrete Research 65, 297–307.
466 Canada, E. and C.C., 2017. Coal phase-out: the Powering Past Coal Alliance [WWW Document]. URL
467 https://www.canada.ca/en/services/environment/weather/climatechange/canada-international-
468 action/coal-phase-out.html (accessed 9.28.21).
469 Cariou, S., Ulm, F.-J., Dormieux, L., 2008. Hardness–packing density scaling relations for cohesive-
470 frictional porous materials. Journal of the Mechanics and Physics of Solids 56, 924–952.
471 de Grazia, M.T., Deda, H., Sanchez, L.F., 2021. The influence of the binder type & aggregate nature on the
472 electrical resistivity of conventional concrete. Journal of Building Engineering 43, 102540.
473 Diamond, S., 2004. The microstructure of cement paste and concrete—a visual primer. Cement and
474 Concrete Composites 26, 919–933. https://doi.org/10/bkmvfx
475 Environment, U., Scrivener, K.L., John, V.M., Gartner, E.M., 2018. Eco-efficient cements: Potential
476 economically viable solutions for a low-CO2 cement-based materials industry. Cement and
477 Concrete Research 114, 2–26. https://doi.org/10/dbmc
478 Fares, G., 2008. Nouveau systèmecimentaire: casde la Frittede verre(New CementitiousSystem: the case of
479 Glass Frit).
480 Faried, A.S., Mostafa, S.A., Tayeh, B.A., Tawfik, T.A., 2021. The effect of using nano rice husk ash of
481 different burning degrees on ultra-high-performance concrete properties. Construction and
482 Building Materials 290, 123279. https://doi.org/10.1016/j.conbuildmat.2021.123279
483 Feng, P., Miao, C., Bullard, J., 2015. Factors Influencing the Stability of AFm and AFt in the Ca - Al - S -
484 O - H System at 25 ° C. Journal of the American Ceramic Society 99, n/a-n/a.
485 https://doi.org/10/f8frnf
486 Feng, S., Wang, P., Liu, X., 2013. SEM-backscattered electron imaging and image processing for
487 evaluation of unhydrated cement volume fraction in slag blended Portland cement pastes. J. Wuhan
488 Univ. Technol.-Mat. Sci. Edit. 28, 968–972. https://doi.org/10/ggkzth
489 Fernandes, I., Broekmans, M.A.T.M., 2013. Alkali–Silica Reactions: An Overview. Part I. Metallography,
490 Microstructure, and Analysis 2. https://doi.org/10/gjg854
491 Fischer-Cripps, A.C., 2004. Nanoindentation Springer. New York.
492 Frech-Baronet, J., Sorelli, L., Charron, J.-P., 2017. New evidences on the effect of the internal relative
493 humidity on the creep and relaxation behaviour of a cement paste by micro-indentation techniques.
494 Cement and Concrete Research 91, 39–51. https://doi.org/10/f9hpsq
495 Goldstein, J., Newbury, D.E., Joy, D.C., Lyman, C.E., Echlin, P., Lifshin, E., Sawyer, L., Michael, J.R.,
496 2003. Scanning Electron Microscopy and X-Ray Microanalysis: Third Edition, 3rd ed. Springer
497 US. https://doi.org/10.1007/978-1-4615-0215-9
498 Gomes, V., Drumond, P.Z., Neto, J.O.P., Lira, A.R., 2016. Co-Processing at Cement Plant of Spent
499 Potlining from the Aluminum Industry, in: Tomsett, A., Johnson, J. (Eds.), Essential Readings in
500 Light Metals: Volume 4 Electrode Technology for Aluminum Production. Springer International
501 Publishing, Cham, pp. 1057–1063. https://doi.org/10.1007/978-3-319-48200-2_142
502 Haha, M.B., De Weerdt, K., Lothenbach, B., 2010. Quantification of the degree of reaction of fly ash.
503 Cement and Concrete Research 40, 1620–1629. https://doi.org/10/fv37rm
504 Holywell, G., Breault, R., 2013. An Overview of Useful Methods to Treat, Recover, or Recycle Spent
505 Potlining. JOM 65, 1441–1451. https://doi.org/10/gfhwkq
506 International Aluminium Institute. Global Mass Flow Mode, 2018.
507 Jain, J., Neithalath, N., 2009. Analysis of calcium leaching behavior of plain and modified cement pastes
508 in pure water. Cement and Concrete Composites 31, 176–185.
509 https://doi.org/10.1016/j.cemconcomp.2009.01.003
510 Khatri, R.P., Sirivivatnanon, V., Gross, W., 1995. Effect of different supplementary cementitious materials
511 on mechanical properties of high performance concrete. Cement and Concrete Research 25, 209–
512 220. https://doi.org/10/b6f9nt
513 Kimmerle, F.M., Kasireddy, V., Tellier, J.G., 2001. SPL treatment by the LCL&L process: Pilot study of
514 two-stage leaching. Light Metals.

515 Kocaba, V., Gallucci, E., Scrivener, K.L., 2012. Methods for determination of degree of reaction of slag in
516 blended cement pastes. Cement and Concrete Research 42, 511–525. https://doi.org/10/fzhz7r
517 Laldji, S., Phithaksounthone, A., Tagnit-Hamou, A., 2010. Synergistic Effect between Glass Frit and Blast-
518 Furnace Slag. ACI Materials Journal 107, 75–79.
519 Laldji, S., Tagnit-Hamou, A., 2007. Glass frit for concrete structures: a new, alternative cementitious
520 material. Canadian Journal of Civil Engineering 34, 793–802. https://doi.org/10/bk2m68
521 L'Hôpital, E., Lothenbach, B., Kulik, D.A., Scrivener, K., 2016. Influence of calcium to silica ratio on
522 aluminium uptake in calcium silicate hydrate. Cement and Concrete Research 85, 111–121.
523 https://doi.org/10/f8txjs
524 Lura, P., Jensen, O.M., Weiss, J., 2009. Cracking in cement paste induced by autogenous shrinkage. Mater
525 Struct 42, 1089–1099. https://doi.org/10/cxhm3d
526 Matschei, T., Lothenbach, B., Glasser, F.P., 2007. The AFm phase in Portland cement. Cement and
527 Concrete Research 37, 118–130. https://doi.org/10/dxh5jn
528 Miller, M., Bobko, C., Vandamme, M., Ulm, F.-J., 2008. Surface roughness criteria for cement paste
529 nanoindentation. Cement and Concrete Research 38, 467–476. https://doi.org/10/bpc9km
530 Mindess, S., 2019. Developments in the Formulation and Reinforcement of Concrete. Woodhead
531 Publishing.
532 Oliver, W.C., Pharr, G.M., 1992. An improved technique for determining hardness and elastic modulus
533 using load and displacement sensing indentation experiments. Journal of Materials Research 7,
534 1564–1583. https://doi.org/10/bdv47f
535 Øye, H.A., 2017. Discussion of Industrial Spent Pot Lining Treatment. 35th International ICSOBA
536 Conference, Hamburg, Germany 8.
537 Poudyal, L., Adhikari, K., 2021. Environmental sustainability in cement industry: An integrated approach
538 for green and economical cement production. Resources, Environment and Sustainability 4,
539 100024. https://doi.org/10.1016/j.resenv.2021.100024
540 Reed, S.J.B., 2005. Electron microprobe analysis and scanning electron microscopy in geology. Cambridge
541 university press.
542 Rustad, I., Karstensen, K.H., Ødegrd, K.E., 2000. Disposal options for spent potlining, in: Woolley, G.R.,
543 Goumans, J.J.J.M., Wainwright, P.J. (Eds.), Waste Management Series, Waste Materials in
544 Construction Wascon 2000. Elsevier, pp. 617–632.
545 Saha, A.K., Khan, M.N.N., Sarker, P.K., Shaikh, F.A., Pramanik, A., 2018. The ASR mechanism of reactive
546 aggregates in concrete and its mitigation by fly ash: A critical review. Construction and Building
547 Materials 171, 743–758.
548 Scrivener, K., Martirena, F., Bishnoi, S., Maity, S., 2017. Calcined clay limestone cements (LC 3). Cement
549 and Concrete Research.
550 Scrivener, K., Snellings, R., Lothenbach, B., 2016. A Practical Guide to Microstructural Analysis of
551 Cementitious Materials. CRC Press.
552 Scrivener, K.L., 2014. Options for the future of cement. Indian Concr. J 88, 11–21.
553 Scrivener, K.L., Patel, H.H., Pratt, P.L., Parrott, L.J., 1986. Analysis of Phases in Cement Paste using
554 Backscattered Electron Images, Methanol Adsorption and Thermogravimetric Analysis. MRS
555 Online Proceedings Library Archive 85. https://doi.org/10/b59fc9
556 Scrivener, K.L., Pratt, P.L., 1984. Backscattered Electron Images Of Polished Cement Sections In The
557 Scanning Electron Microscope. Proceedings of the International Conference on Cement
558 Microscopy 145–155.
559 Shahsavari, R., Buehler, M.J., Pellenq, R.J.-M., Ulm, F.-J., 2009. First-principles study of elastic constants
560 and interlayer interactions of complex hydrated oxides: Case study of tobermorite and jennite.
561 Journal of the American Ceramic Society 92, 2323–2330.
562 Sorelli, L., Vallée, D., Alizadeh, A.R., Beaudoin, J., Randall, N., 2012. Disclosing the mechanical
563 properties of green calcium-silicate-hydrates by statistical nanoindentation techniques, in:
564 Advanced Materials Research. Trans Tech Publ, pp. 544–549.

565 Soroka, I., Abayneh, M., 1986. Effect of gypsum on properties and internal structure of PC paste. Cement
566 and Concrete Research 16, 495–504. https://doi.org/10/c4trfm
567 Talero, R., Pedrajas, C., González, M., Aramburo, C., Blázquez, A., Rahhal, V., 2017. Role of the filler on
568 Portland cement hydration at very early ages: Rheological behaviour of their fresh cement pastes.
569 Construction and Building Materials 151, 939–949. https://doi.org/10/ghn3w9
570 Taylor, H.F.W., 1997. Cement chemistry, 2nd ed. ed. T. Telford, London.
571 The SPL Waste Management Challenge in Primary Aluminum, 2021. . Light Metal Age Magazine. URL
572 https://www.lightmetalage.com/news/industry-news/smelting/the-spl-waste-management-
573 challenge-in-primary-aluminum/ (accessed 4.4.22).
574 Thomas, M.D.A., 1989. The suitability of solvent exchange techniques for studying the pore structure of
575 hardened cement paste. Advances in Cement Research 2, 29–34.
576 https://doi.org/10.1680/adcr.1989.2.5.29
577 Ulm, F.-J., Vandamme, M., Bobko, C., Ortega, J.A., Tai, K., Ortiz, C., 2007. Statistical Indentation
578 Techniques for Hydrated Nanocomposites: Concrete, Bone, and Shale. Journal of the American
579 Ceramic Society 90, 2677–2692. https://doi.org/10/czhw6g
580 Ulm, F.-J., Vandamme, M., Jennings, H.M., Vanzo, J., Bentivegna, M., Krakowiak, K.J., Constantinides,
581 G., Bobko, C.P., Van Vliet, K.J., 2010. Does microstructure matter for statistical nanoindentation
582 techniques? Cement and Concrete Composites 32, 92–99. https://doi.org/10/cq28qh
583 Vandamme, M., 2008. The nanogranular origin of concrete creep : a nanoindentation investigation of
584 microstructure and fundamental properties of calcium-silicate-hydrates.
585 Vandamme, M., Ulm, F.-J., 2013. Nanoindentation investigation of creep properties of calcium silicate
586 hydrates. Cement and Concrete Research 52, 38–52. https://doi.org/10/f5f4zk
587 Vanzo, J., 2010. A nanochemomechanical investigation of carbonated cement paste.
588 Vijayakumar, G., Vishaliny, H., Govindarajulu, D., 2013. Studies on Glass Powder as Partial Replacement
589 of Cement in Concrete Production. undefined.
590 Wei, J., Ma, S., Thomas, D., 2016. Correlation between hydration of cement and durability of natural fiber-
591 reinforced cement composites. Corrosion Science 106.
592 https://doi.org/10.1016/j.corsci.2016.01.020
593 Wei, Y., Liang, S., Gao, X., 2017. Indentation creep of cementitious materials: Experimental investigation
594 from nano to micro length scales. Construction and Building Materials 143, 222–233.
595 https://doi.org/10/ggkmkj
596 Wilson, W., Sorelli, L., Tagnit-Hamou, A., 2018a. Unveiling micro-chemo-mechanical properties of C–
597 (A)–S–H and other phases in blended-cement pastes. Cement and Concrete Research 107, 317–
598 336. https://doi.org/10/gdhsr7
599 Wilson, W., Sorelli, L., Tagnit-Hamou, A., 2018b. Automated coupling of NanoIndentation and
600 Quantitative Energy-Dispersive Spectroscopy (NI-QEDS): A comprehensive method to disclose
601 the micro-chemo-mechanical properties of cement pastes. Cement and Concrete Research 103, 49–
602 65. https://doi.org/10/gcwq6m
603 Zajac, M., Rossberg, A., Le Saout, G., Lothenbach, B., 2014. Influence of limestone and anhydrite on the
604 hydration of Portland cements. Cement and Concrete Composites 46, 99–108.
605 https://doi.org/10/ggrbdh
606 Zhang, Q., Le Roy, R., Vandamme, M., Zuber, B., 2014. Long-term creep properties of cementitious
607 materials: Comparing microindentation testing with macroscopic uniaxial compressive testing.
608 Cement and Concrete Research 58, 89–98. https://doi.org/10/gg3w35
609

610

611

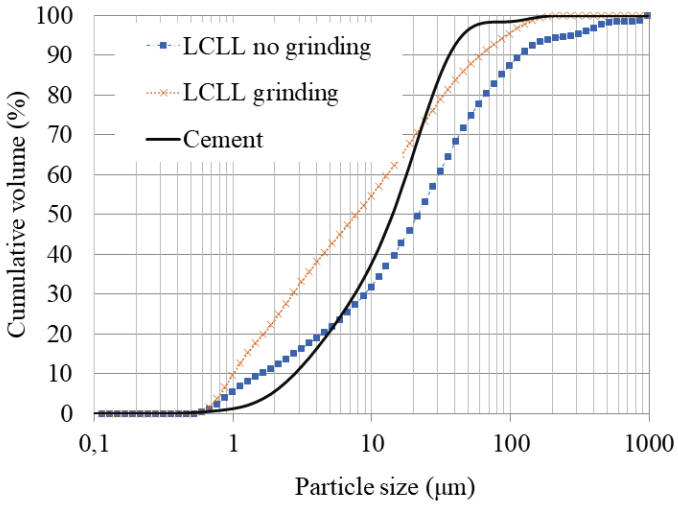

612
613 **Fig. 1**. PSD of cement and LCLL-ash.

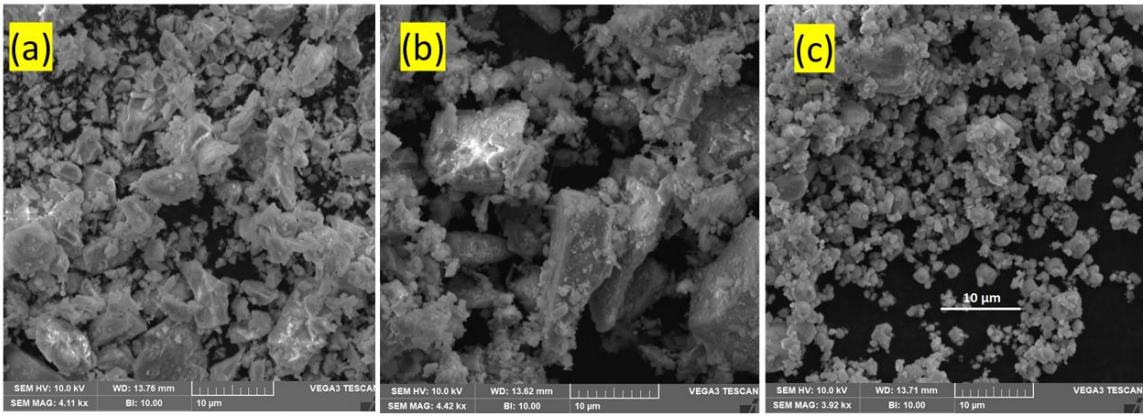

614

615 **Fig. 2**. SEM micrographs of (a) cement, (b) LCLL-ash, and (c) anhydrite.

616

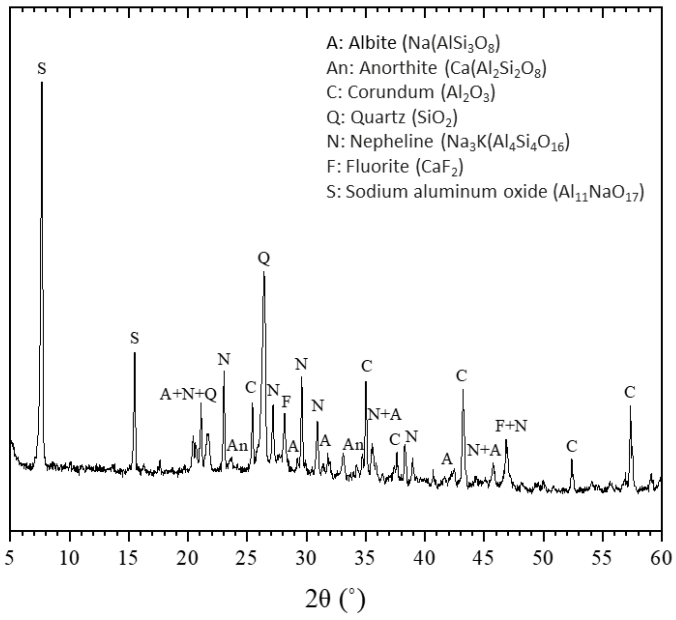

617

618 **Fig. 3**. X-ray diffraction patterns of LCLL-ash.

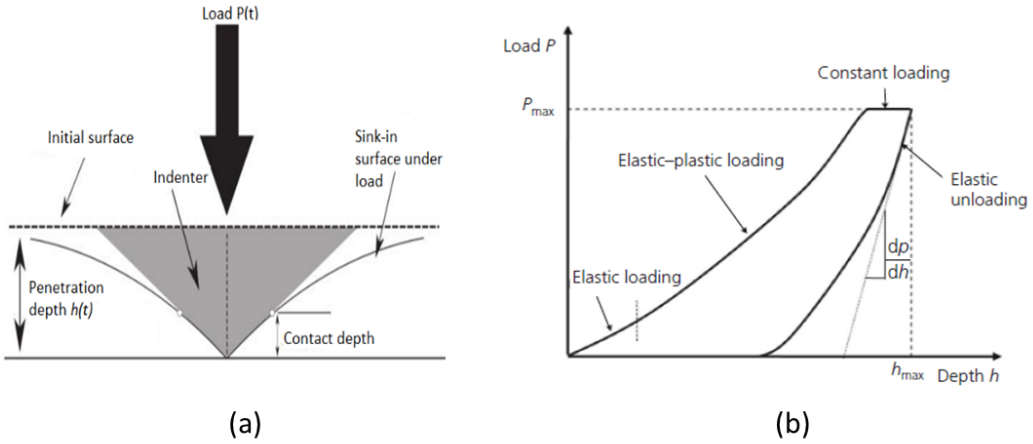

619

620 **Fig. 4**. A schematic view of the indentation load-displacement curve (a) sectional view of the

621 physical parameter under load, (b) load-deformation curve (Frech-Baronet et al., 2017).

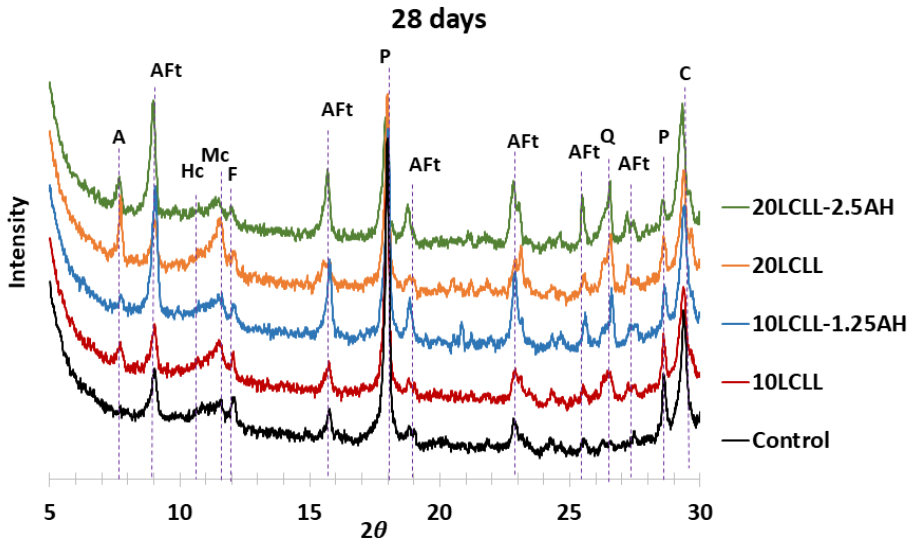

622

623 **Fig. 5**. X-ray diffraction patterns of pastes at 28 days. Mc—monocarboaluminate, P—portlandite, C—

624 Calcite, AFt—ettringite, F—Ferrite, Hc—hemicarboaluminate, Q—quartz, A— Sodium aluminate oxide.

625

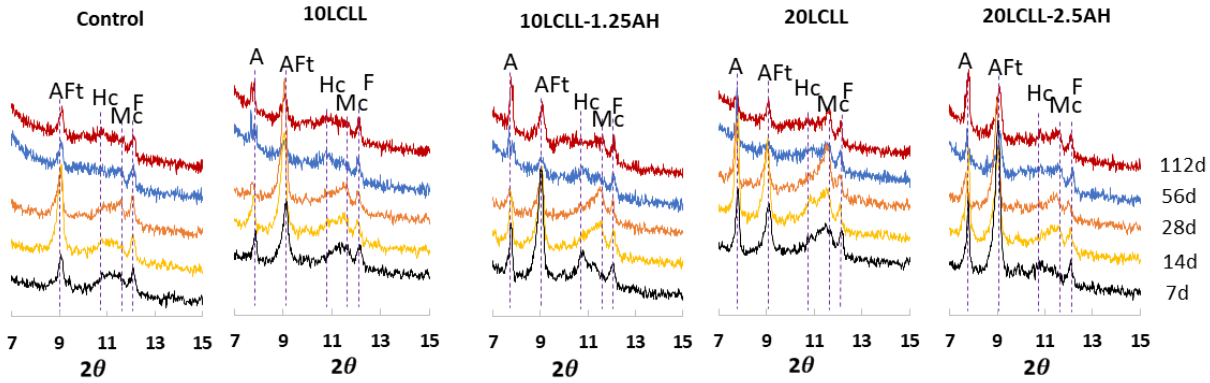

626

627 **Fig. 6**. X-ray diffraction patterns of all investigated samples at difference days: Mc—

628 monocarboaluminate, Hc—hemicarboaluminate, AFt—ettringite, F—Ferrite, A — Sodium aluminate

629 oxide.

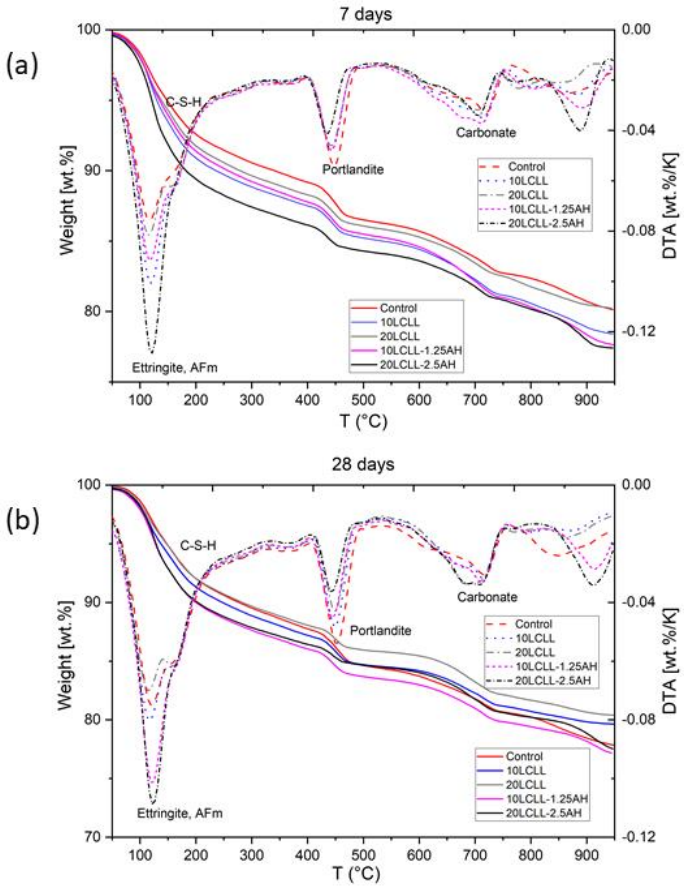

630

631 **Fig. 7.** DTA/ TG curves of hydrated cement paste samples at (a) 7 days and (b) 28 days.

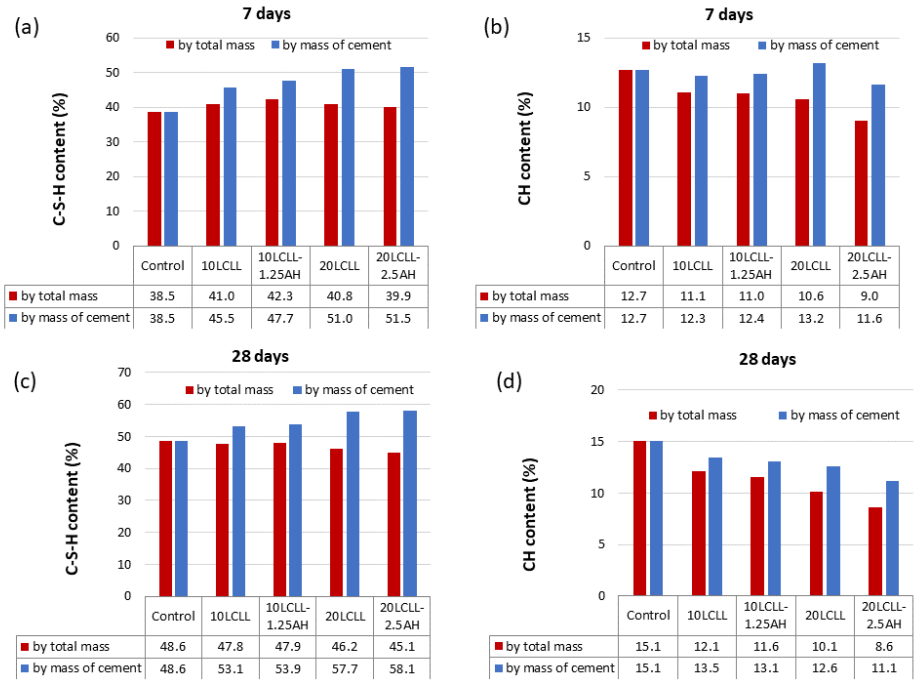

Fig. 8. C-S-H content at (a) 7 days and (c) 28 days and CH content at (b) 7 days and (d) 28 days as determined from the TG curves.

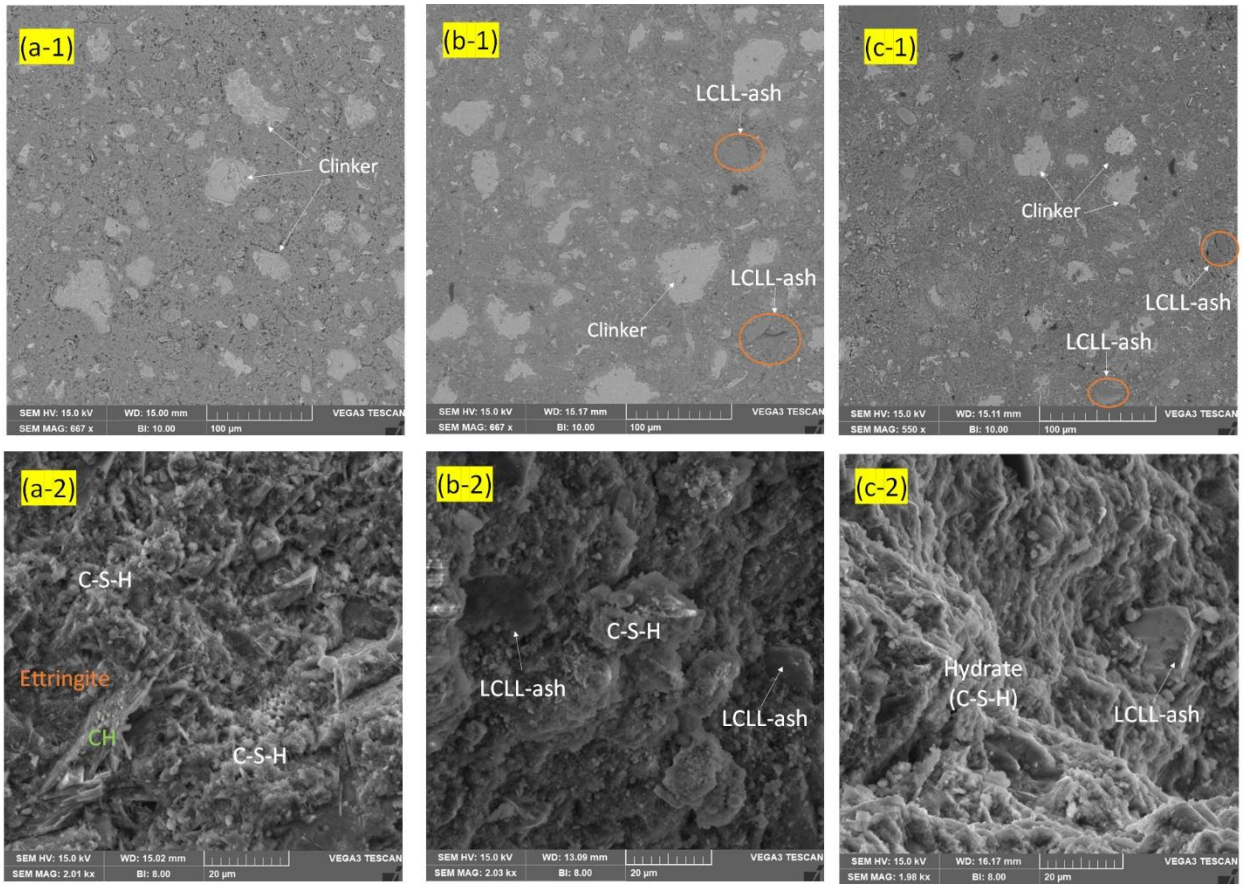

635

636 **Fig. 9**. BSE images of 28-day curing. (a) Control; (b) 10LCLL; and (c) 20LCLL.

637

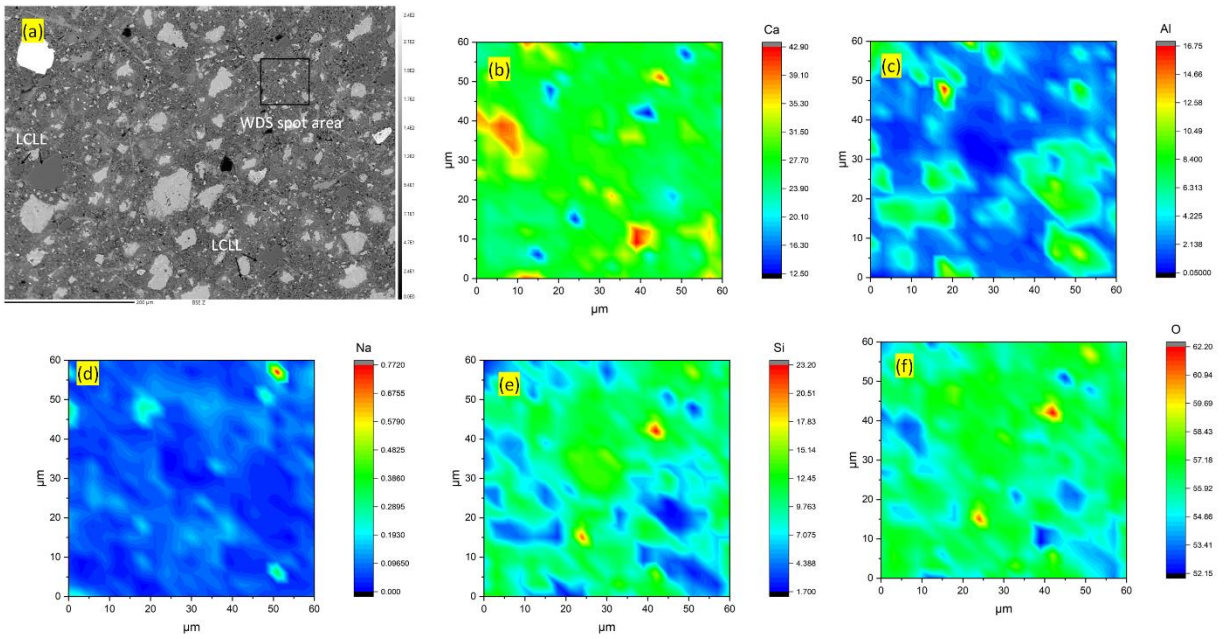

638

639 **Fig. 10**. Quantitative WDS elemental mapping of 10LCLL sample at 28 days of curing with scale weight

640 percentage (wt.%) for (a) BSE image, (b) calcium, (c) aluminum, (d) sodium, (e) silicon and (f) oxide.

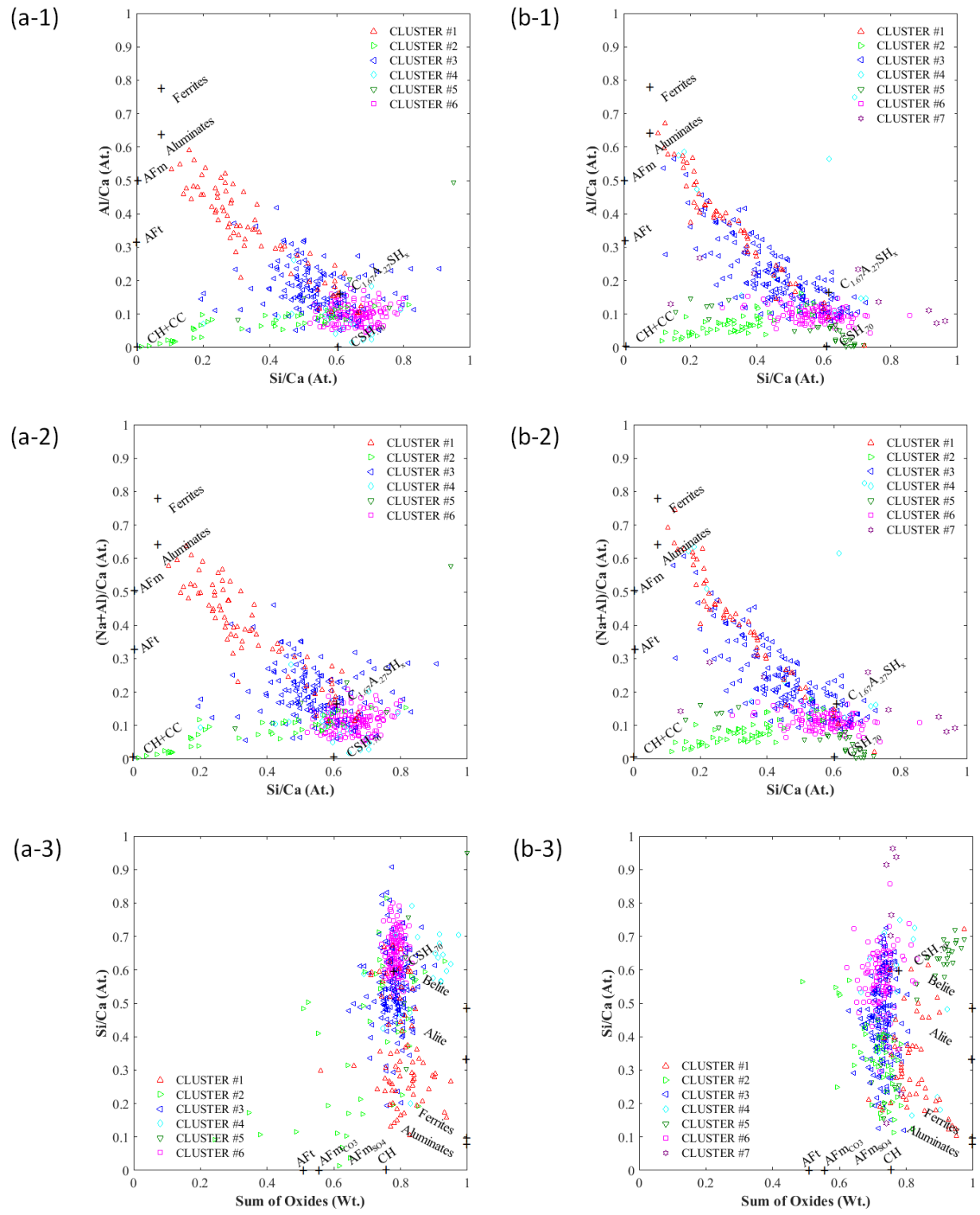

641

642 **Fig. 11**. Statistical clustering analysis for the (a) Control and (b) 10LCLL in terms of (a-1,b-1) (Fe+Al)/Ca

643 vs. Si/Ca; (a-2,b-2) (Na+Al)/Ca vs. Si/Ca and (a-3,b-3) Si/Ca vs. Sum of Oxides (SOX).

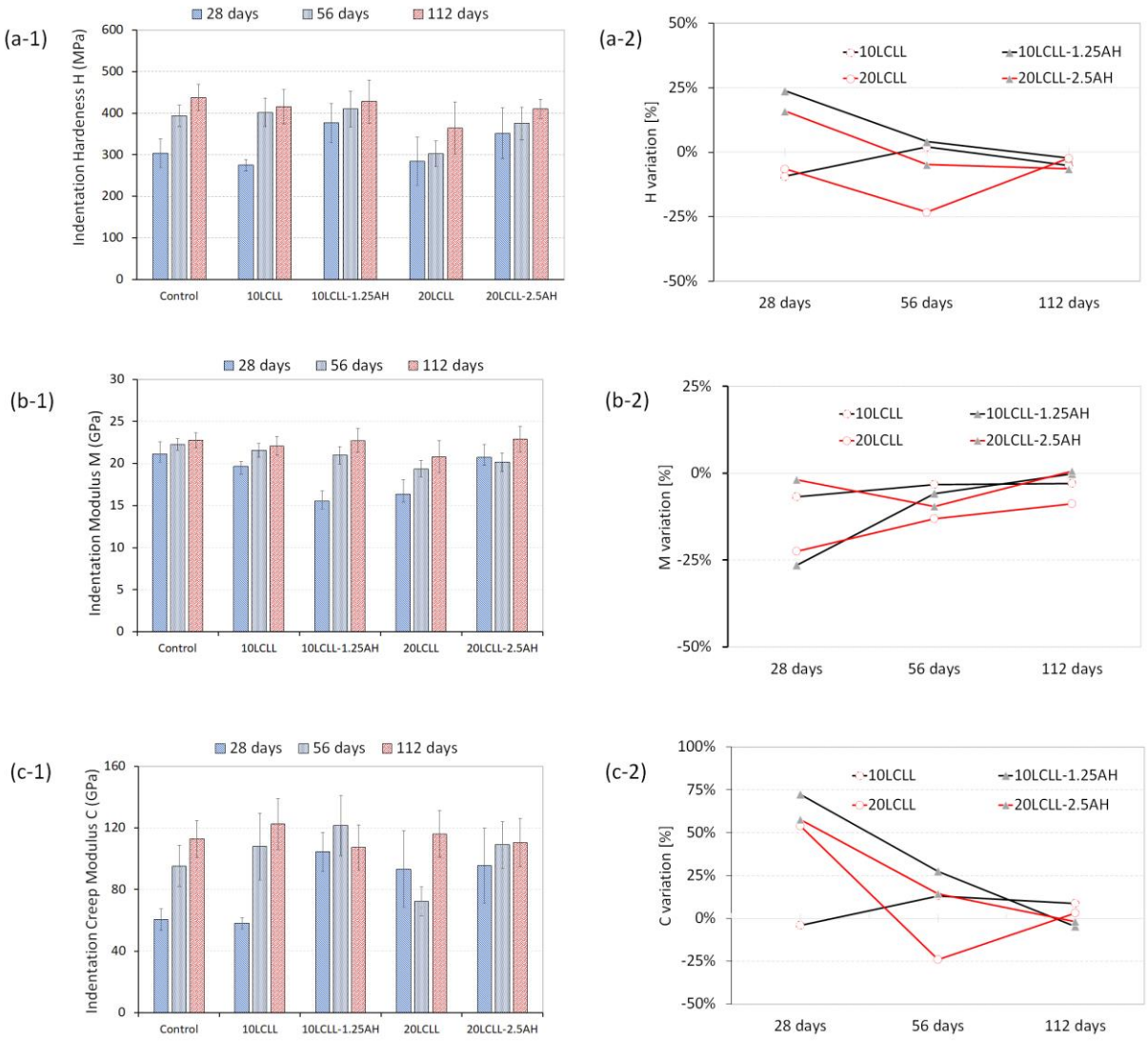

Fig. 12. Micromechanical properties of cement pastes: (a-1) Indentation Hardness H; (b-1) Indentation Modulus M; and (c-1) Indentation Creep Modulus C. Normalized micromechanical properties to control sample: (a-2) Indentation Hardness H; (b-2) Indentation Modulus M; and (c-2) Indentation Creep Modulus C.

653 **Table 1**. Chemical properties (wt.%) and physical properties of cement and LCLL-ash

	Cement	LCLL-ash
Chemical properties (wt.%)		
CaO	60.20	3.04
SiO_2	19.13	37.18
Al_2O_3	4.80	36.29
Fe_2O_3	3.60	7.37
SO_3	3.80	0.07
MgO	2.6	0.38
TiO_2	0.23	0.73
Na_2O	0.25	8.23
P_2O_5	0.19	0.12
K_2O	1.1	0.77
Mn_2O_3	0.07	-
Physical properties		
LOI	1.92	5.72
Specific gravity (g/cm^3)	3.09	2.72
Blaine's fineness (m^2/kg)	395	-
Surface area m^2/g (BET)	-	4.6

654

655 **Table 2.** Mix proportion in mass of different OPC-LCLL-ash blended cement paste

Name of samples	Cement [%]	LCLL-ash [%]	Anhydrite [%]	w/b [-]	w/c [-]
Control	100.00	/	/	0.35	0.35
10LCLL	90.00	10	/	0.35	0.38
10LCLL-1.25AH	88.75	10	1.25	0.35	0.39
20LCLL	80.00	20	/	0.35	0.43
20LCLL-2.5AH	77.50	20	2.50	0.35	0.45

656

657

658 **Table 3**. Results of the chemical clustering by quantitative chemistry from WDS for the Control sample

Cluster	Si/Ca (At.)	(Fe+Al)/Ca (At.)	S/Ca (At.)	Mg/Ca (At.)	SOX (Wt.)	π (%)	Predominant phases
#1	0.37 ± 0.16	0.41 ± 0.16	0.09 ± 0.03	0.13 ± 0.06	0.80 ± 0.06	19	Aluminate Mix
#2	0.41 ± 0.22	0.09 ± 0.04	0.06 ± 0.02	0.03 ± 0.01	0.70 ± 0.14	10	CH + C-S-H
#3	0.54 ± 0.11	0.21 ± 0.08	0.09 ± 0.03	0.07 ± 0.03	0.78 ± 0.04	30	Al-rich + C-S-H
#4	0.59 ± 0.12	0.11 ± 0.07	0.04 ± 0.03	0.18 ± 0.20	0.87 ± 0.07	4	Silicates Mix
#5	0.63 ± 0.22	0.24 ± 0.17	0.09 ± 0.02	0.02 ± 0.01	0.85 ± 0.07	2	Others
#6	0.65 ± 0.05	0.12 ± 0.03	0.08 ± 0.02	0.06 ± 0.03	0.78 ± 0.02	35	Mostly C-S-H

659

660 **Table 4**. Results of the chemical clustering by quantitative chemistry from WDS for the 10LCLL sample

Cluster	Si/Ca (At.)	(Fe+Al)/Ca (At.)	S/Ca (At.)	Mg/Ca (At.)	SOX (Wt.)	π (%)	Predominant phases
#1	0.33 ± 0.14	0.48 ± 0.21	0.05 ± 0.03	0.13 ± 0.06	0.82 ± 0.06	12	Aluminate Mix
#2	0.34 ± 0.12	0.08 ± 0.04	0.05 ± 0.02	0.02 ± 0.01	0.71 ± 0.06	12	CH + C-S-H
#3	0.45 ± 0.13	0.26 ± 0.11	0.08 ± 0.02	0.07 ± 0.03	0.73 ± 0.03	36	Al-rich + C-S-H
#4	0.50 ± 0.2	0.56 ± 0.45	0.09 ± 0.06	0.46 ± 0.41	0.79 ± 0.06	3	Silicates Mix
#5	0.55 ± 0.17	0.06 ± 0.05	0.01 ± 0.01	0.02 ± 0.01	0.88 ± 0.08	6	Others
#6	0.58 ± 0.08	0.11 ± 0.03	0.07 ± 0.02	0.03 ± 0.01	0.73 ± 0.03	27	Mostly C-S-H
#7	0.92 ± 0.66	0.22 ± 0.15	0.06 ± 0.02	0.13 ± 0.02	0.77 ± 0.03	4	Mostly LCLL

661

662 **Table 5**. ANOVA results on Indentation Modulus M, Hardness H with significant level $\alpha = 0.05$. To reject
663 the null hypothesis with confidence, P values must be smaller than 0.01 and F must be larger than F_{crit}

Curing days	Indentation Modulus M		Indentation Hardness H		
	P	F	P	F	F_{crit}
28 days	3.39703E-57	90.37	1.52557E-35	50.32	2.39
56 days	7.35718E-71	170.96	3.84858E-44	89.78	2.62
112 days	3.43703E-57	123.37	1.72537E-35	70.34	2.40

664